ADVENGMAT
Vol. 18 – No. 11
November, 2016

ADVANCED ENGINEERING MATERIALS

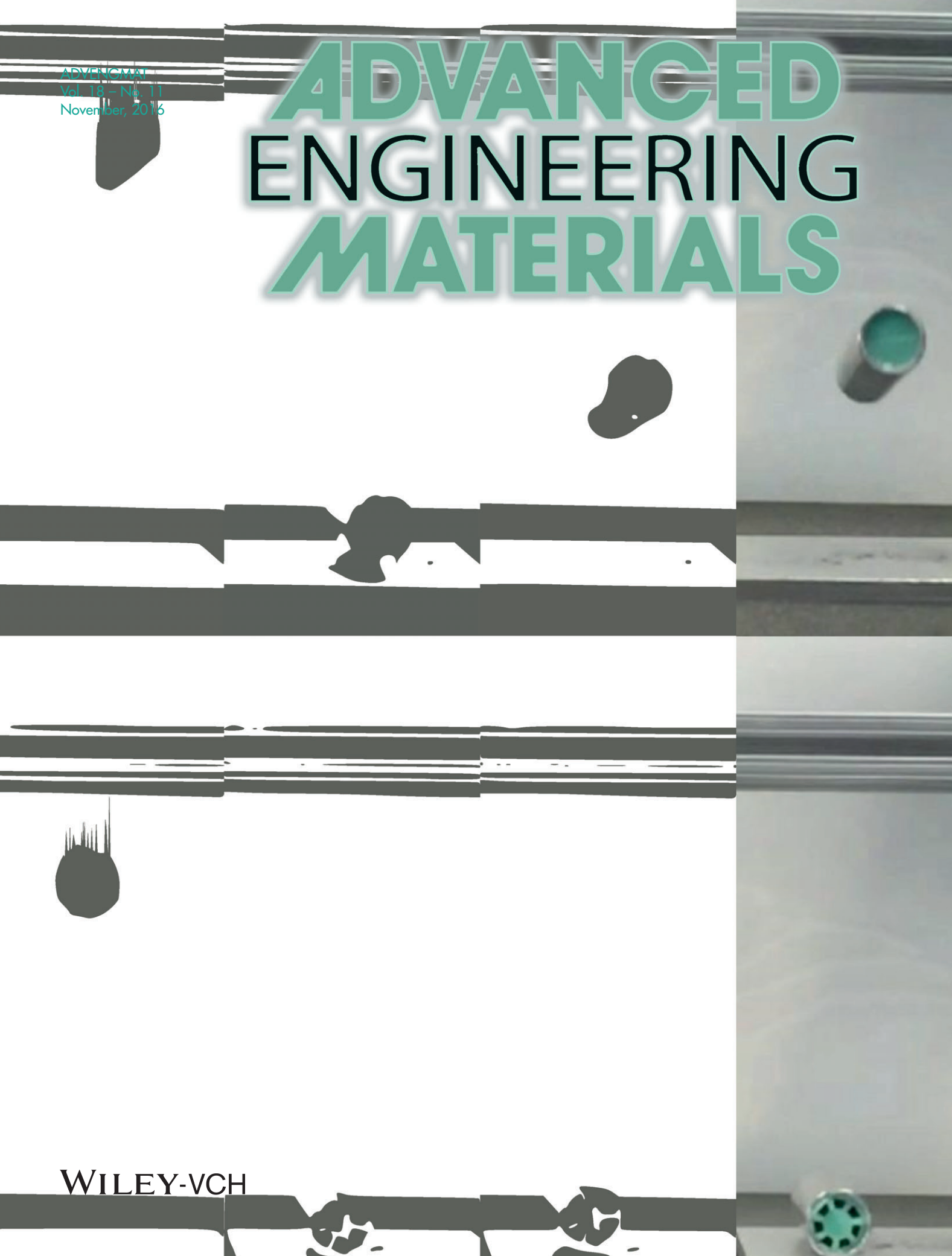

WILEY-VCH

ADVANCED ENGINEERING MATERIALS

wileyonlinelibrary.com

Visit our homepage at:
http://www.aem-journal.de

CONTENTS

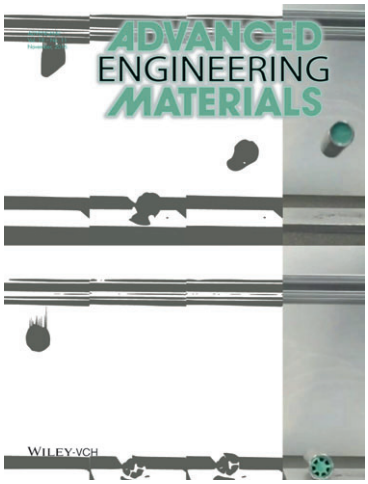

Strategically architected elastomeric materials constrained near critical points yield extreme impact energy absorption for structures in which they are embedded. This image includes high-speed video stills of drop experiments conducted to quantify the impact energy attenuation provided by specimens for the shells into which the specimens are inserted. Architected and strategically constrained specimens (bottom row) more greatly suppress impact energy than the bulk material itself (top row). Further details can be found in the article by Ryan Harne and co-workers on page 1871.

Review

Three Decades of Auxetics Research – Materials with Negative Poisson's Ratio: A Review

K. K. Saxena, R. Das, E. P. Calius*

Adv. Eng. Mater. **2016,** *18*, 1847–1870

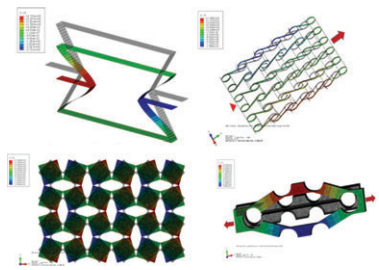

Auxetic materials possess an interesting property of negative Poisson's ratio. By virtue of this negative Poisson's ratio, several other mechanical properties can be enhanced. This review presents briefly the current state of the art and progress in the auxetics research made in the past three decades. The review attractively covers most of the aspects of auxetic materials such as classification, structure, properties, applications, design, and modeling.

Communications

Resilience to Impact by Extreme Energy Absorption in Lightweight Material Inclusions Constrained Near a Critical Point

*J. Bishop, Q. Dai, Y. Song, R. L. Harne**

Adv. Eng. Mater. **2016,** *18*, 1871–1876

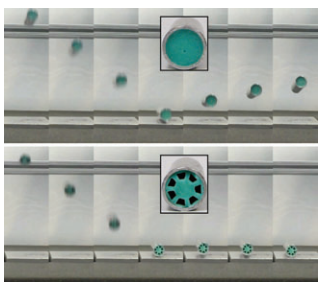

Strategically architected elastomeric materials constrained near critical points yield extreme impact energy absorption for structures in which they are embedded. The concepts and model elastomer architecture devised here motivate ideas for reusable protective structures and shock-resilient systems.

Tailoring Toughness and Mechanical Reliability by Controlled Defects: Nature-Inspired Composite Laminates of Laser-Perforated Yttria-Stabilized Zirconia

*S. Behr, A. Köllner, G. A. Schneider**

Adv. Eng. Mater. **2016,** *18*, 1877–1883

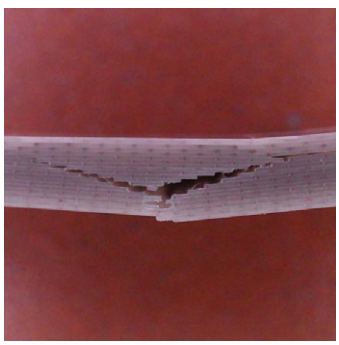

The high strength of ceramic materials scatters with the distribution of natural defects and design limits are often far beyond experimentally determined values. This issue can be resolved by controlled defect generation in laminates, leading to composites that are as strong as monolithic ceramics but significantly more reliable and damage tolerant.

CONTENTS

Isothermal wetting kinetics of liquid aluminum on solid boron compounds (AlB_2, B_4C, CaB_6, MgB_2, TiB_2) are investigated at typical aluminum casting temperatures and are quantified in terms of the contact angle. No wetting (contact angles <90°) occurs at testing conditions, but for B_4C and AlB_2 the contact angle decreases over time.

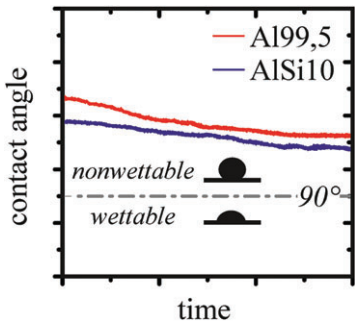

Wettability of Low Weight Borides by Commercial Aluminum Alloys – A Basis for Metal Matrix Composite Fabrication

S. Ploetz, R. Nowak, A. Lohmueller, N. Sobczak, R. F. Singer*

Adv. Eng. Mater. **2016,** *18*, 1884–1888

Full Papers

Fe–Ni–P ternary alloys are fabricated using core–shell structured Fe–Ni–P composite powder at lower sintering temperature. The specimens sintered at 950 and 975 °C can obtain the ultra-fine micro-structure and avoid the eutectic compounds precipitating along grain boundaries. Results illustrate that this micro-structure is beneficial to the mechanical properties of alloys.

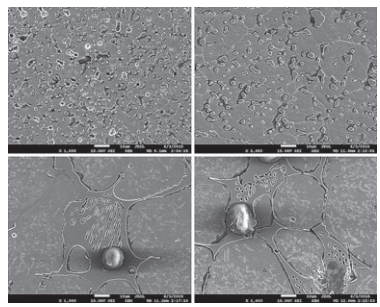

Preparation and Properties of High Strength Fe–Ni–P Ternary Alloys

*W. Chai, R. M. German, E. A. Olevsky, X. Wei, R. Jiang, G. Cui**

Adv. Eng. Mater. **2016,** *18*, 1889–1896

The influence of CNT defects, distributed both randomly and in clusters, on the electrical conductivity of CNT/polymer composites is investigated considering covalent bonds as electrical resistors. The composite electrical conductivity with different fractions of CNT defects and orientations are modeled through the composite cylinder and Mori–Tanaka's methods. The composite electrical conductivity decreased about 30% for an 8% fraction of defects.

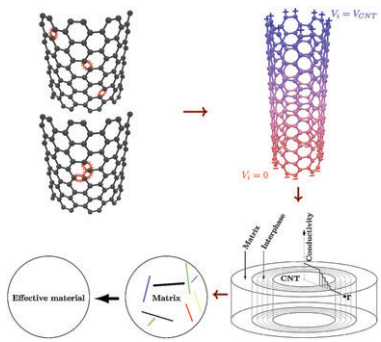

Influence of Structural Defects on the Electrical Properties of Carbon Nanotubes and Their Polymer Composites

*G. Domínguez-Rodríguez, A. Tapia, G. D. Seidel, F. Avilés**

Adv. Eng. Mater. **2016,** *18*, 1897–1905

Hybrid composite including carbon nanotube sheets and carbon fiber prepregs is in situ cured by applying electrical current to carbon nanotube layers. The relationship between input current and composite temperature is explored. Fully cured samples show low void content and good storage modulus. In situ curing is demonstrated as energy saving technique to fabricate multifunctional composite.

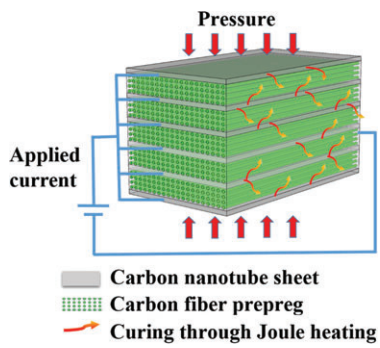

In Situ Curing and Out-of-Autoclave of Interply Carbon Fiber/Carbon Nanotube Buckypaper Hybrid Composites Using Electrical Current

N. Nguyen, A. Hao, J. G. Park, R. Liang*

Adv. Eng. Mater. **2016,** *18*, 1906–1912

Preparation and Interface Investigation of Fe/Al_2O_{3P} Composite Activated by Ni and Ti

S. L. Tang, Y. M. Gao, Y. F. Li, Q. L. Zheng*

Adv. Eng. Mater. **2016,** *18*, 1913–1920

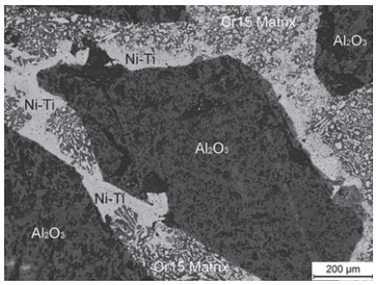

Ceramic particle preforms are synthesized by vacuum sintering reaction between Al_2O_3 particles and Ni–Ti complex powders. Then the Cr15 matrix composite is fabricated by infiltration casting process. The preforms sintered by Al_2O_3 and Ni–Ti have high compressive strength, and the three-body abrasive wear resistance of composite is over 12 times higher than Cr15.

Improved Properties of Carbon Nanotube-Fluorhydroxyapatite Biocomposite: Mechanical, Chemical Stability, and Antibacterial Activity

Y.-L. Bai, Y. Bai, W. Ma, R.-L. Jia, X.-B. Zheng*

Adv. Eng. Mater. **2016,** *18*, 1921–1929

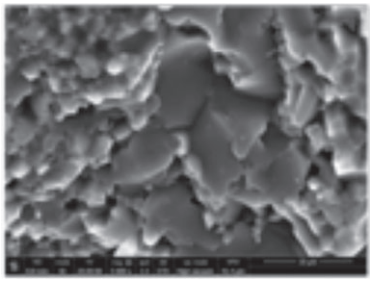

The carbon nanotubes/fluoridated hydroxyapatite (CNTs/FHA) composite is fabricated by an in situ chemical synthesis method and spark plasma sintering technology. The composite shows improved mechanical properties, chemical stability, in vitro bioactivity, and antibacterial properties as compared with pure HA materials.

Synthesis of Molybdenum and Niobium Mono- and Binary Silicides by the Method of SHS-Metallurgy

*V. Yukhvid, V. Gorshkov, P. Miloserdov, N. Skachkova, M. Alymov, G. Nolze, A. Epishin**

Adv. Eng. Mater. **2016,** *18*, 1930–1935

Mono- and binary silicides Mo–Nb–Si with different ratios of Nb/Mo are synthesized from the highly exothermic mixtures of MoO_3, Nb_2O_5, Si, and Al by the method of SHS-metallurgy.

Tough TiB_2-Based Ceramic Composites Using Metallic Glass Powder as the Sintering Aid

C. Yang, Y. Yao, Y. Huan, Z. Fu, F. Chen, E. J. Lavernia**

Adv. Eng. Mater. **2016,** *18*, 1936–1943

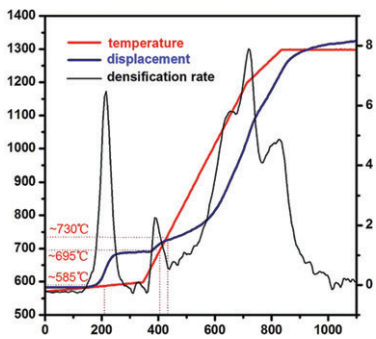

The authors report on the formation of toughened TiB_2-based ceramic composites using metallic glass powder as sintering aid fabricated by spark plasma sintering. The TiB_2 ceramic powder blended with 5 wt% metallic glass sintering aid exhibits an interesting sigmoidal shrinkage behavior. The fabricated TiB_2-based ceramic composites have high fracture toughness of 9.9 $MPam^{1/2}$. The results provide a novel pathway for fabrication of high-performance ceramic composites.

The oxidation behavior of three different zones of linear friction welded Ti_2AlNb alloy is studied. For base metal, absorption of more oxygen due to higher amount of α_2 phase leads to the thickest oxidation scale, while the preferential formation of Al_2O_3 for joint is beneficial to the oxidation resistance. However, along with the formation of $AlNbO_4$ phase after long exposure in air, the oxidation behavior of the three zones has become similar.

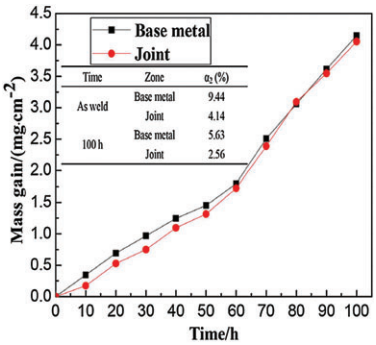

Oxidation Behavior of Three Different Zones of Linear Friction Welded Ti_2AlNb Alloy

X. Chen, F. Q. Xie, T. J. Ma, W. Li, X. Q. Wu*

Adv. Eng. Mater. **2016,** *18*, 1944–1951

The thermomechanical properties of two MAX Phases, Ti_3SiC_2 and Ti_2AlC, sintered via spark plasma sintering method are investigated. Ultrasound pulse echography permitted to follow the evolution of Young's modulus up to 1623 K. Additionally, AE activity during heating (up to 1473 and 1632 K) and cooling stages is recorded.

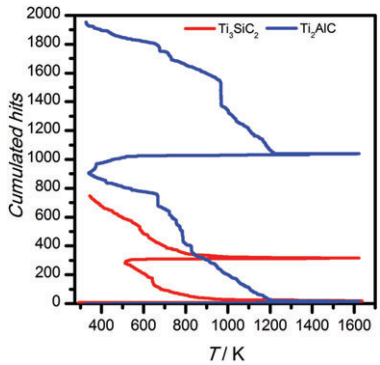

Characterization of Thermomechanical Behavior of Ti_3SiC_2 and Ti_2AlC Ceramics Elaborated by Spark Plasma Sintering Using Ultrasonic Means

K. Kozak, A. Dosi, G. Antou,* N. Pradeilles, T. Chotard**

Adv. Eng. Mater. **2016,** *18*, 1952–1957

This study reports the creep behavior of hot pressed unmilled AlMg5, milled AlMg5, and AlMg5 powders milled with 0.5 vol% of Al_2O_3 nanoparticles. The nanocomposite AlMg5–0.5Al_2O_3 shows superior room temperature tensile properties and higher creep deformation compared to unmilled samples.

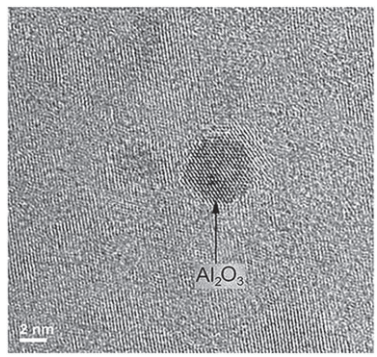

Microstructure, Mechanical, and Impression Creep Properties of AlMg5–0.5 vol% Al_2O_3 Nanocomposites

M. K. Talari, N. Kishore Babu, K. Kallip, M. Leparoux, R. E. Koller, K. A. AlOgab, X. Maeder*

Adv. Eng. Mater. **2016,** *18*, 1958–1966

SiC_f/SiC composites are joined to Hastelloy N alloys using 82.5Au–17.5Ni (wt%) foil as brazing filler. The brazing temperature and holding time have a great influence on the microstructure and shear strength of the joints. Nanocrystalline graphite, Ni_2Si, and $Ni_{31}Si_{12}$ are formed in brazed seams.

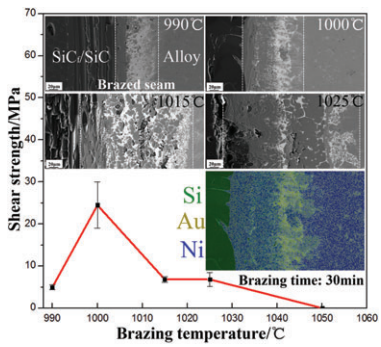

Microstructural Evolution and Mechanical Properties of 2D–SiC_f/SiC and Hastelloy N Joints Using 82.5Au–17.5Ni Brazing Filler

M. Liu, X. Yang, H. Zhou, Y. Gao,* H. Xia,* P. Huai, X. Zhou, Y. Lu*

Adv. Eng. Mater. **2016,** *18*, 1967–1973

ADVANCED ENGINEERING MATERIALS

DOI: 10.1002/adem.201600501

Resilience to Impact by Extreme Energy Absorption in Lightweight Material Inclusions Constrained Near a Critical Point**

By *Justin Bishop, Quanqi Dai, Yu Song* and *Ryan L. Harne**

This work investigates a model design for lightweight, architected material inclusions that cultivate significant impact energy dissipation in structures. The inclusions are sustained near a critical point where damping is theoretically increased without bound. Using the principle, a material architecture and constraint mechanism are studied that exemplify the theory. Guided by a computational model and analysis, numerous specimens are fabricated and experimentation verifies that engineered material inclusions constrained nearer to critical points most effectively suppress structural dynamics following impact, minimize transmitted impulsive force, and better promote structural integrity. The concepts articulated here may find broad application for reusable, resilient protective structures.

Left unabated, impact energy can result in extraordinary harm to engineered systems and the delicate objects contained therein. Recent attention on sports- and service-related head injuries[1] has directed significant effort to develop new material systems for helmets with unprecedented impact mitigation capabilities[2] that may serve as models for a wider class of energy-absorbing materials. Beyond head injuries, everyday engineering structures including aircraft, automobiles, and civil infrastructure, to name a few, must be resilient enough to withstand unexpected blast or impact loading without compromising the safety and integrity of occupants and cargo.[3,4]

These motivations have fueled research communities for decades, particularly to devise materials with the ideal balance of high damping and high stiffness.[5–11] Among the investigations, the use of negative stiffness has been postulated to engender significant energy absorption by virtue of phase transformation phenomena and the associated hysteretic damping effects.[12–15] Such transitions have been induced in composite matter using ferroelectric[16] and temperature[17,18] tuning, showing that macroscopic stiffness and damping are controllable across orders of magnitude with respect to the bulk composite properties in absence of tuning.[13,19] Designs for architected, elastomeric, or mechanical metamaterials incorporating two- or multi-state transformations have also been presented to absorb, "trap," or rectify vibration and wave energy via topological transitions among stable equilibria.[20–24] Such metamaterials bring the ideas from composite matter closer to practical embodiments by virtue of innovative designs and implementations.

These more practical metamaterial concepts that exploit negative stiffness and phase transformations indeed demonstrate significant energy dissipation, including for impact absorption. Yet, in agreement with the prior developments in studies on two-phase matter,[12,19] the transitions themselves are not the preferred tools to leverage for extreme energy dissipation. To exemplify this reasoning, consider an example from structural mechanics. The fundamental generalized coordinate of (bending) motion for a simply supported beam is denoted w, Figure 1a. A negative stiffness, respecting transverse beam deflection w, is introduced by applying a compressive force P along the beam axis; a non-dimensional parameter p is proportional to this force, $p \propto P$.[25] For variation in the compressive force, the lowest, linear eigenfrequency ω_n vanishes at the critical point $p = 1$, which

[*] *Dr. R. L. Harne, J. Bishop, Q. Dai, Y. Song*
Department of Mechanical and Aerospace Engineering, The Ohio State University, Columbus, Ohio 43210, USA
E-mail: harne.3@osu.edu

[**] *R. L. H. acknowledges start-up funds from the Department of Mechanical and Aerospace Engineering at The Ohio State University (OSU). Q. D. acknowledges support from the OSU College of Engineering Honors Research Scholarship. A provisional U.S. patent (62/302,405) has been filed on ideas described in this report. (Supporting Information is available online from Wiley Online Library or from the author).*

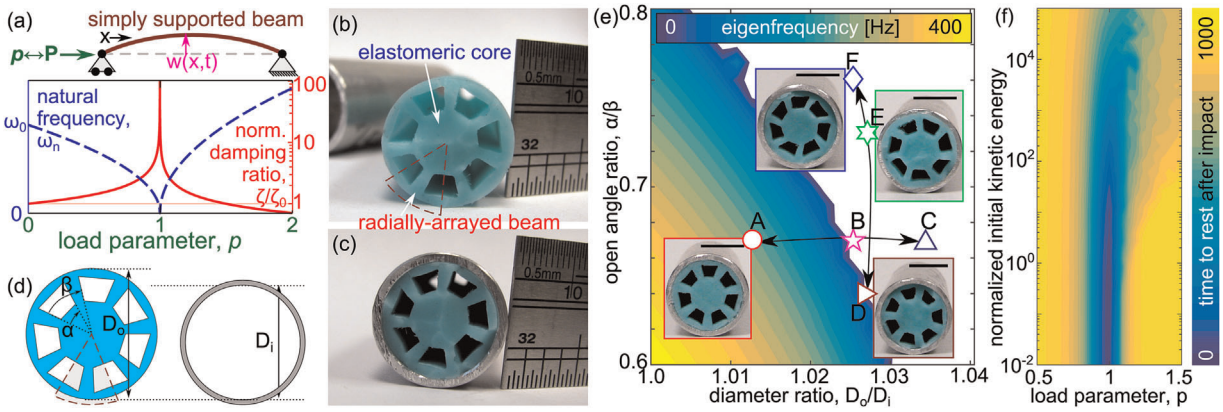

Fig. 1. Concepts and material design methods. (a) Illustration of critical point in an axially compressed beam resulting in unbounded damping ratio. (b) Material inclusion without constraint, and (c) under constraint within the cylindrical structure. (d) Inclusion design parameters considered in FE model, with the FE model geometry shown at the left. (e) FE model results of lowest eigenfrequency sensitivity to parameter change. The unshaded area denotes post-buckled inclusions while the horizon between shaded and unshaded areas is the range of parameters promoting the critical point: the effective condition that $p = 1$. In (e) inset photographs, the black bars are 10 mm. (f) Analytical prediction of time for a structure to return to rest after being acted upon by an initial energy for various inclusions having different load parameters p.

separates pre- ($p \leq 1$) and post-buckled ($p > 1$) beam configurations. The damping ratio is determined by $\zeta = b/(2m\ \omega_n)$ where b and m are, respectively, the inherent material viscous damping and the mass associated with the generalized coordinate w. By virtue of this definition, the damping ratio ζ increases without bound *at the critical point*; the solid curve plotted in Figure 1a presents this dependence when normalized against the damping ratio without the force ζ_0. In general, for values of p near to the critical point $p \approx 1$, the damping ratio ζ is orders of magnitude greater than when the force is removed $p = 0$ or when the beam is post-buckled $p > 1$, while imperfections and system asymmetries reduce the maximum growth of damping.[26] Analogous phenomena to this example in mechanics are elsewhere observed in ecology, physiology, finance, and other sciences as reported by a "critical slowing down"[27,28] which is indicative of enhanced "damping" effects acting on the ordinary time scale of dynamics. Building from such reasoning, we hypothesize that the most effective strategy by which to leverage phase transitions in architected material systems for extreme damping properties is not to trigger post-buckling behaviors like the recent elastomeric and mechanical metamaterial concepts,[20–24] but is instead a strategy to sustain the engineered materials at the critical point itself.

In this report, we investigate this hypothesis by probing a model realization of a lightly damped, elastomeric, and architected material inclusion that is constrained on the verge of buckling when embedded within a structural system, Figure 1b and c and see Supporting Information. Guided by computational and analytical models that illuminate strategies for design and implementation of such inclusions, we experimentally characterize the roles of critical point constraints on the effectiveness of suppressing impact energy and transmitted impulse to the structure within which the architected material inclusion is embedded and constrained. The focus on impact energy dissipation capability in this study is motivated by its prime importance in numerous applications[3,4] and by its valuable characterization of broadband damping performance.[2] In addition, our examination of linear-like damping properties aims to challenge the potential for critical point constraints to facilitate robust impact energy absorption that may be free from the amplitude-dependence of contemporary nonlinear systems considered to promote exceptional energy damping and diffusion.[20–24] The following paragraphs describe our approaches, findings, and conclusions.

Compressive stress,[29] geometric constraint,[23] and active multi-field tuning[16,17,30–32] are candidate methods for sustaining material systems near phase transitions. We capitalize on a passive, geometric constraint applied to an architected elastomer material inclusion, Figure 1b and c. The rotationally symmetric, radially arrayed beam geometry, outlined in the dashed line in Figure 1b and c, is inspired by recent work on post-buckled metamaterials.[33] In contrast to the prior work, here a cylindrical structure to-be-dampened constrains the radially arrayed beams of the elastomer inclusion by virtue of the fact that the inclusion outer diameter D_o is slightly greater than the inner diameter D_i of the cylindrical shell. This geometric constraint yields a strategic compressive stress near the critical point of buckling for the radially arrayed beams, such that the lowest linear eigenfrequency of the inclusion vanishes in the ideal case. The torsional and radial motions of the elastomeric core provide the lumped mass displacements to bend the beams under this constraint. Thus, the inherent viscous dissipation of radially arrayed beam bending is the baseline damping capacity that is amplified in consequence to the critical point constraint provided by the shell.

This inclusion architecture was recently investigated by the authors in a different context of vibroacoustic wave trapping and attenuation within poroelastic media that served as hosts to such inclusions.[34] By virtue of the "hidden" degree-of-freedom (i.e., a constrained inclusion), the poroelastic metamaterials exhibited large vibration and wave damping particularly in

resonance frequency bands associated with the poroelastic media stiffness and the mass and geometry of the inclusion and shell. Focusing strictly and more closely in this report at the broadband damping enhancement provided to the shell structural dynamics by the constrained inclusion itself, here we first utilize the previously developed, plane strain finite element (FE) model[34] of the architected elastomer inclusion to derive new insights. The FE model assesses the parametric influences that tailor the lowest eigenfrequency and cause it to vanish at the ideal critical point; additional model details are given in the Supporting Information. For this inclusion topology, as depicted by the FE model geometry in Figure 1d, the open-to-closed angle ratio α/β and the diameter ratio D_o/D_i of the symmetric unit cell are key non-dimensional parameters by which the inclusions are tuned near to the critical point where the lowest eigenfrequency becomes zero. From the new FE model results shown in Figure 1e, the critical point $p = 1$ is the horizon between shaded and unshaded areas, uncovering a substantially larger design space for critical point constraints than that identified in the previous work.[34]

We fabricate and prepare inclusions across the design space shown in the contour plot of Figure 1e (and see Video File 1). We report on results obtained using the representative cases shown as the data markers in the contour. The inset photographs of Figure 1e exemplify the influences of change in the non-dimensional parameters. Large α/β produces slender radially arrayed beams, which can give rise to buckling evident by inclusion rotation,[33,34] shown for specimens E and F. According to our hypothesis the inclusions labeled B and D will be those with the greatest energy dissipation capabilities, since they exhibit the smallest values of fundamental eigenfrequency according to the FE model results, Figure 1e. Indeed, our corresponding analysis of a simplified two-dimensional system verifies that impact energy is most effectively suppressed in a structure that contains an inclusion constrained at the critical point $p = 1$ such that the inclusion natural frequency vanishes, see Supporting Information. The analytical model predicts, seen in Figure 1f, that following an initial impulsive energy input, the structure with an inclusion nearest the critical point ($p \approx 1$) returns to rest in several orders-of-magnitude less time than either pre- ($p < 1$) or post-buckled ($p > 1$) inclusions. This is additional evidence that elimination of restoring forces relatively amplifies the dissipative influences on the system dynamics, providing a potent means for impact energy suppression. The aim of our experimental efforts is to assess the efficacy of such seemingly simple theory.

To first evaluate the damping performance of the architected material inclusions when compared to baselines, we conduct drop experiments using cylindrical shell specimens, shell specimens filled with bulk elastomer, and specimens with architected inclusions, see the insets of Figure 2a and b and Supporting Information. A laser sensor measures specimen displacement in a sufficiently long time duration around impact to accurately determine incoming and outgoing specimen speeds. A force transducer below the thick impact plate measures the transmitted impulse received by the cylindrical structure.

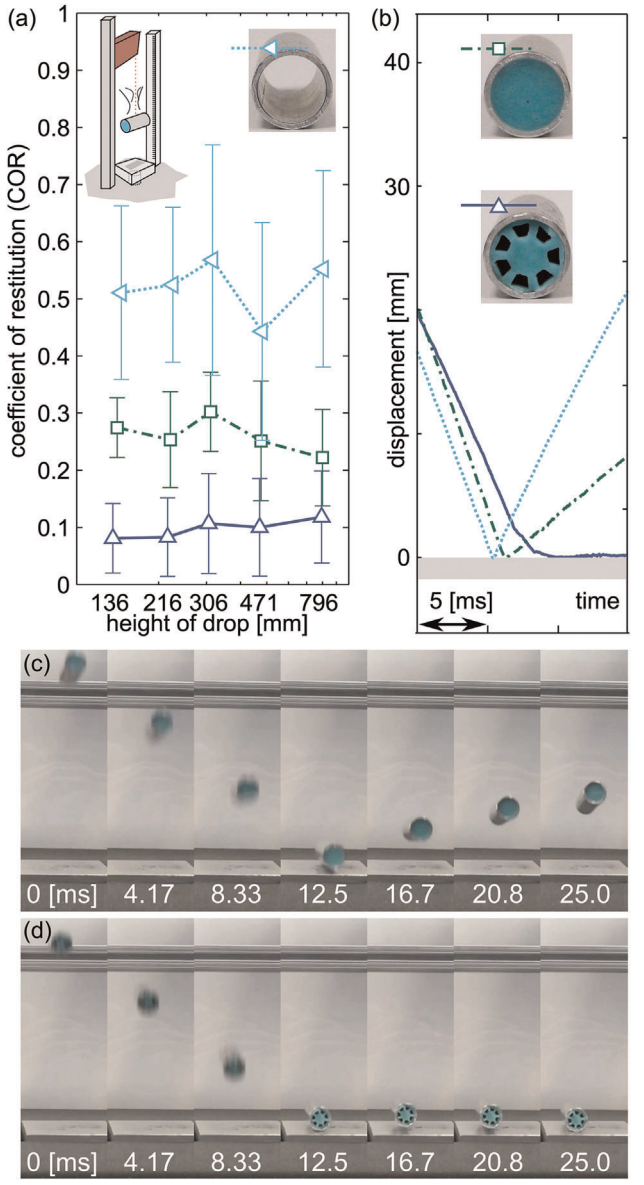

Fig. 2. Evidence of impact energy attenuation from drop experiments. (a) Means (points) and standard deviations (bars) of measurements for drop tests taken for the cylindrical shell, shell with bulk elastomer, and shell with material inclusion constrained in the vicinity of the critical point. (b) Representative time series for the three specimens when dropped from 471 [mm] and video snap-shots for specimens with (c) bulk elastomer and a (d) material inclusion.

Hunt and Crossley[35] observed that the coefficient of restitution ($\mathrm{COR} = v_o/v_i$, with v_o and v_i being outgoing and incoming speeds, respectively) could serve as a useful proxy for impact energy attenuation, where smaller COR values represent larger energy absorption. Figure 2a presents the COR data from the drop experiments, while Figure 2b–d and Video File 2 provide representative displacement time series of impact events. The high mean COR for the aluminum shell is evidence of its low damping and inherent inability to absorb impact energy. Comparatively, the introduction of bulk elastomer reduces COR to approximately 60% of the shell

COMMUNICATION

baseline. Yet, the increased energy dissipation is insufficient to inhibit all rebound, Figure 2c, while the bulk elastomer has the disadvantage that the net specimen mass is doubled. In striking contrast, the architected material inclusion reduces the COR to approximately 20% or less of the shell baseline, thus preserving the integrity of the structure into which it is embedded, Figure 2d. Importantly, the material inclusion is also 33% less massive than the bulk elastomer. Thus, with less mass the material inclusion absorbs substantially greater energy and preserves the structure from excessive rebound (see Video File 2). This verifies that strategic constraint near a critical point can introduce considerable damping, in accordance with the analytical prediction given in Figure 1f.

To assess the efficacy of the hypothesis grounding our approach, the measurements from drop experiments using specimens with material inclusions that cover the parameter space shown in Figure 1e are presented in Figure 3. Specimens A, B, and C have the same angle ratio α/β, but the diameter ratios D_o/D_i are, respectively, less than, very near, and beyond that required to achieve the critical point. Figure 3a shows that specimen B, sustained nearest to the critical point, exhibits the most significant suppression of impact energy by virtue of the smallest mean COR (8.76%) across the five heights from which the specimens are dropped; this compares to specimen A (mean COR 10.1%) and specimen C (mean COR 9.73%). Such relative performance is predicted according to the basis of achieving maximal energy dissipation for inclusions nearest to the point of buckling. In Figure 3b, we compare the COR measurements for specimens D, E, and F, which, respectively, possess inclusions on the verge of buckling, post-buckled, and still further post-buckled, by change of the angle ratio α/β with nearly identical diameter ratios. The inset photographs of Figure 1e show the specimens and how the post-buckled

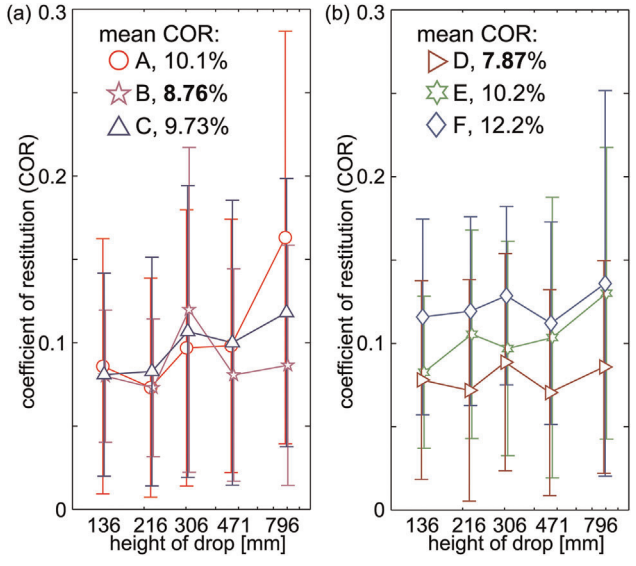

Fig. 3. Enhanced impact energy attenuation by material inclusion design near the critical point. COR measurements are shown for specimens (a) A, B, C that vary diameter ratio and for specimens (b) D, E, F that vary angle ratio. Means (points) and standard deviations (bars) are shown, as a function of the drop height. The overall mean COR values are provided for each specimen at the top of the respective sub-figure.

rotation of the inclusion is evident by the increase in α/β from D to E, and then exacerbated from E to F. As revealed by our measurements, Figure 3b, the specimens with post-buckled inclusions E and F are inferior at suppressing the impact energy because the mean COR values are, respectively, 10.2 and 12.2% compared to the inclusion D constrained nearest to the critical point with mean COR 7.87%. The collective evidence first verifies that the critical point is the origin of extreme impact energy absorption. Second, the results demonstrate that specimen F is less effective at damping the structural dynamics upon impact than the less buckled specimen E, which is in agreement with the premise upon which this research bases its motivation to achieve the most effective attenuation of impact energy. Moreover, considering both specimen groups, the COR does not significantly increase for the range of drop heights examined, although the impulsive energy increases by more than 5.8 times across this range. When compared to metamaterials that exploit phase transitions associated with triggering required thresholds,[20–22] the damping capability realized by our material design concept near the phase transition is more robust to changing input energy amplitudes (i.e., a linear-like property) in accordance with the principle and theory underlying the phenomenon.

Finally, mitigating impact energy to protect structures and delicate contents therein requires that impulsive forces/stresses transmitted to the bodies are minimized;[1,2] minimizing this stress also promotes reusability of a protective structure. In our investigation, the relevant metric to minimize is the impact force measured beneath the impact plate. Figure 4 presents the measurements of peak impact force for the cylindrical shell itself and with the bulk elastomer, alongside measurements for (a) specimen group A, B, and C, and for (b) specimen group D, E, and F. The specimen utilizing bulk elastomer results in peak impact forces approximately 150% greater than the rest of cases considered, although it is 121% of the mean mass of the specimens that possess constrained material inclusions. This indicates that the bulk elastomer does not provide the same extent of impulsive force suppression per mass that the material inclusions empower by virtue of the strategic architecture and constraint. Within statistical measures, the architected material inclusions all result in similar peak impulsive forces according to the height at which the specimens are dropped. These impulsive forces are comparable to those measured for the shell itself, despite the fact that the specimens with constrained inclusions are approximately 70% more massive than the shell alone. Consequently, the acceleration imparted to the shell by the impact force is approximately 70% less for the specimens that utilize the material inclusions compared to the shell on its own. Summarizing the findings, the structural specimens with architected inclusions undergo smaller impact forces, increased energy attenuation, and more rapid elimination of the structural dynamics via the constraint near the critical point. Additional experimentation on a broader range of specimens

ADVANCED ENGINEERING MATERIALS

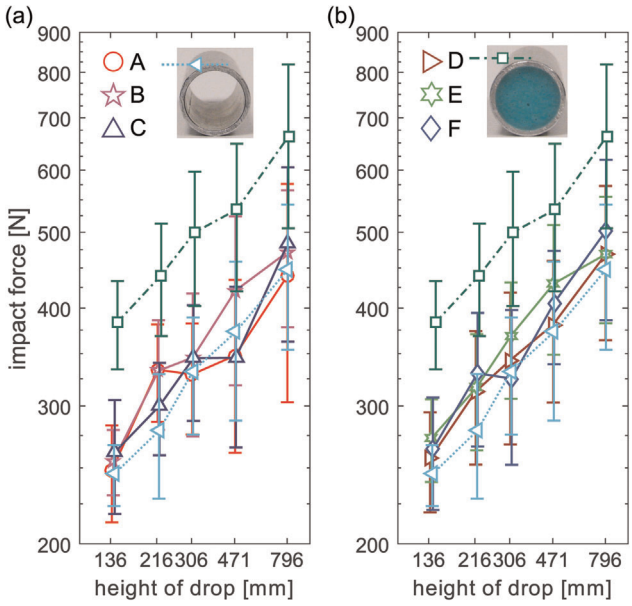

Fig. 4. Impact force from drop experiments. Comparison of specimens with shell alone and the shell with bulk elastomer to measurements for specimens (a) A, B, and C, and (b), D, E, and F. Means (points) and standard deviations (bars) are shown, as a function of the drop height.

and constraint configurations corroborates such findings (see Supplementary Information).

Our results draw important, new conclusions regarding the use of critical points of transition in engineered material systems as means to cultivate extreme impact energy absorption for resilient structures. Although recent research is identifying promising approaches to leverage phase transformations in metamaterial systems,[20–24] the implementation of a phase transition necessarily requires storage and release of energy. This results in the opportunity that energy may be undesirably returned to the system, i.e., via "snap-back" events.[20] Contrasting such approach, our ideal material inclusions exhibit purely resistive impedance since the contribution of dissipative forces is maximized simultaneously as restoring forces are minimized.[26]

In addition, unlike the sensitivities of activating phase transformations[20] and key roles of initial conditions,[25] the concept described here is extremely repeatable (see Video File 2). Our analysis anticipates that the rapid suppression of impact energy is not linearly scalable to ever-increasing energy inputs for the ideally constrained inclusions, shown in Figure 1f and Supporting Information. On the other hand, using the design approach established here, one may use the FE model guidance to select appropriate inclusion material and architected topology that promote the required constraints and grant the needed energy dissipation. Nevertheless, we have conducted drop experiments beginning from 136 [mm] to 5.8 [m] (see Video File 3) that do not cause plastic deformation to the shell, and the results are consistent with our premise.

In summary, our approach to elastomeric material architecture and constraint achieves significant and rapid attenuation of impact energy for the structures in which such inclusions are applied. The idea is clearly extensible to other inclusion designs and structural implementations. As shown by our model specimens, the concept is easy to manufacture and assemble. In applications where impact energy must be rapidly absorbed by a resilient structure to prevent harm to delicate cargo and ensure long-term structural integrity, we conclude that deploying a material on the verge of a critical transition provides the most effective and expedited elimination of energy.

Article first published online: August 29, 2016
Manuscript Revised: August 11, 2016
Manuscript Received: July 12, 2016

[1] V. E. Johnson, W. Stewart, D. H. Smith, *Exp. Neurol.* **2013**, *246*, 35.
[2] T. Rahimzadeh, E. M. Arruda, M. D. Thouless, *J. Mech. Phys. Solids* **2015**, *85*, 98.
[3] P. Du Bois, C. C. Chou, B. B. Fileta, T. B. Khalil, A. I. King, H. F. Mahmood, H. J. Mertz, J. Wismans, *Vehicle Crashworthiness and Occupant Protection*, American Iron and Steel Institute, Southfield, Michigan **2004**.
[4] G. J. McShane, S. M. Pingle, V. S. Deshpande, N. A. Fleck, *Int. J. Solids Struct.* **2012**, *49*, 2830.
[5] M. Brodt, R. S. Lakes, *J. Compos. Mater.* **1995**, *29*, 1823.
[6] Z. Xue, J. W. Hutchinson, *Int. J. Impact Eng.* **2004**, *30*, 1283.
[7] J. Meaud, T. Sain, B. Yeom, S. J. Park, A. B. Shoultz, G. Hulbert, Z. D. Ma, N. A. Kotov, A. J. Hart, E. M. Arruda, A. M. Waas, *ACS Nano* **2014**, *8*, 3468.
[8] J. Meaud, T. Sain, G. M. Hulbert, A. M. Waas, *Int. J. Solids Struct.* **2013**, *50*, 1342.
[9] C. S. Andreasen, E. Andreassen, J. S. Jensen, O. Sigmund, *J. Mech. Phys. Solids* **2014**, *63*, 228.
[10] L. R. Meza, S. Das, J. R. Greer, *Science* **2014**, *345*, 1322.
[11] K. C. Cheung, N. Gershenfeld, *Science* **2013**, *341*, 1219.
[12] R. S. Lakes, T. Lee, A. Bersie, Y. C. Wang, *Nature* **2001**, *410*, 565.
[13] D. M. Kochmann, *Mech. Res. Commun.* **2014**, *58*, 36.
[14] W. J. Drugan, *Phys. Rev. Lett.* **2007**, *98*, 055502.
[15] B. Florijn, C. Coulais, M. van Hecke, *Phys. Rev. Lett.* **2014**, *113*, 175503.
[16] C. S. Wojnar, J. B. le Graverend, D. M. Kochmann, *Appl. Phys. Lett.* **2014**, *105*, 162912.
[17] Y. C. Wang, M. Ludwigson, R. S. Lakes, *Mater. Sci. Eng. A* **2004**, *370*, 41.
[18] T. Jaglinski, D. Kochmann, D. Stone, R. S. Lakes, *Science* **2007**, *315*, 620.
[19] F. Fritzen, D. M. Kochmann, *Int. J. Solids Struct.* **2014**, *51*, 4101.
[20] S. Shan, S. H. Kang, J. R. Raney, P. Wang, L. Fang, F. Candido, J. A. Lewis, K. Bertoldi, *Adv. Mater.* **2015**, *27*, 4296.
[21] D. Restrepo, N. D. Mankame, P. D. Zavattieri, *Extreme Mech. Lett.* **2015**, *4*, 52.

[22] D. M. Correa, T. Klatt, S. Cortes, M. Haberman, D. Kovar, C. Seepersad, *Rapid Prototyping J*. **2015**, *21*, 193.
[23] R. L. Harne, Z. Wu, K. W. Wang, *J. Mech. Des*. **2016**, *138*, 021402.
[24] N. Nadkarni, A. F. Arrieta, C. Chong, D. M. Kochmann, C. Daraio, *Phys. Rev. Lett*. **2016**, *116*, 244501.
[25] L. N. Virgin, *Vibration of Axially Loaded Structures*, Cambridge University Press, Cambridge **2007**.
[26] L. N. Virgin, R. Wiebe, *Philos. Trans. R. Soc. A* **2013**, *371*, 20120426.
[27] M. Scheffer, J. Bascompte, W. A. Brock, V. Brovkin, S. R. Carpenter, V. Dakos, H. Held, E. H. van Nes, M. Rietkerk, G. Sugihara, *Nature* **2009**, *461*, 53.
[28] M. Scheffer, S. R. Carpenter, T. M. Lenton, J. Bascompte, W. Brock, V. Dakos, J. van de Koppel, I. van de Leemput, S. A. Levin, E. H. van Nes, M. Pascual, J. Vandermeer, *Science* **2012**, *338*, 344.
[29] S. Shan, S. H. Kang, P. Wang, C. Qu, S. Shian, E. R. Chen, K. Bertoldi, *Adv. Funct. Mater.* **2014**, *24*, 4935.
[30] D. Yang, L. Jin, R. V. Martinez, K. Bertoldi, G. M. Whitesides, Z. Suo, *Extreme Mech. Lett*. **2016**, *6*, 1.
[31] K. Singh, C. R. Tipton, E. Han, T. Mullin, *Proc. R. Soc. A* **2013**, *469*, 20130111.
[32] M. Schaeffer, M. Ruzzene, *Int. J. Solids Struct*. **2015**, *56–57*, 78.
[33] P. Wang, F. Casadei, S. Shan, J. C. Weaver, K. Bertoldi, *Phys. Rev. Lett*. **2014**, *113*, 014301.
[34] R. L. Harne, Y. Song, Q. Dai, *Extreme Mech. Lett*. **2016**, doi: 10.1016/j.eml.2016.05.017
[35] K. H. Hunt, F. R. E. Crossley, *J. Appl. Mech*. **1975**, *42*, 440.

Supporting Information

for *Adv. Mater*., DOI: 10.1002/adem.201600501

Title: Resilience to Impact by Extreme Energy Absorption in Lightweight Material Inclusions Constrained near a Critical Point

*Authors: Justin Bishop, Quanqi Dai, Yu Song, and Ryan L. Harne**

1. Analytical model formulation and results

By a modal analysis or Galerkin approach, the primary shell and inclusion dynamic responses may be modeled as a two degree-of-freedom (DOF) system, and schematically visualized using the lumped-parameter constituents shown in Figure S1. The effective mass m_1 is associated with the fundamental mass of the shell, according to a primary generalized coordinate of motion x, here referred to as the "structure response". The effective mass m_2 is likewise determined for the fundamental oscillation response v of the material inclusion, here referred to as the "inclusion response". The primary stiffness and viscous damping of the shell are k_1 and b_1, respectively. The terms k_2, k_3 are the linear and nonlinear stiffnesses of the material inclusion, and b_2 is the inherent viscous damping constant associated with the response v. The linear stiffness k_2 is adjusted by virtue of the significance of inclusion compression within the shell. The nonlinear stiffness k_3 must be accounted for because as the linear stiffness vanishes, $k_2 \to 0$, finite applied force would induce infinite inclusion response v in the absence of other restoring potentials. Thus, the nonlinear stiffness k_3 is associated with large displacements from an equilibrium and, in the general framework of the material inclusions considered here, is associated with large

bending of the radially-arrayed beams while the linear stiffness of the material inclusion k_2 is associated with the primary beam bending generalized coordinate [25].

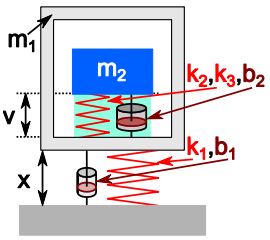

Figure S1. Schematic of two DOF system with tunable stiffness k_2 associated with constraints.

The governing equations of motion for the system shown in Figure S1 are derived using Newton's second law of motion

$$m_1\ddot{x}+b_1\dot{x}+k_1x-b_2\dot{v}-k_2(1-p)v-k_3v^3=0 \tag{1}$$

$$m_2(\ddot{v}+\ddot{x})+b_2\dot{v}+k_2(1-p)v+k_3v^3=0 \tag{2}$$

where the load parameter p is proportional to the constraint that opposes the inherent linear stiffness k_2 of the inclusion and results in buckling [25]. Upon introducing the terms

$$f=\omega_2/\omega_1;\ \omega_2^2=k_2/m_2;\ \omega_1^2=k_1/m_1;\ \gamma_1=b_1/m_1\omega_1;\ \gamma_2=b_2/m_2\omega_2 \tag{3}$$

$$\mu=m_2/m_1;\ \tau=\omega_1 t;\ \partial/\partial t=\omega_1(\partial/\partial\tau)=\omega_1(\ )';\ \beta=k_3/k_2 \tag{4}$$

we nondimensionalize the equations (1) and (2) to yield

$$x''+\gamma_1x'+x-\mu f\gamma_2v'-\mu f^2(1-p)v-\mu f^2\beta v^3=0 \tag{5}$$

$$v''+(1+\mu)f\gamma_2v'+(1+\mu)f^2(1-p)v+(1+\mu)f^2\beta v^3-\gamma_1x'-x=0 \tag{6}$$

We investigate equations (5) and (6) for the dependence of the system free response in consequence to various initial values, $(x_0,\dot{x}_0,v_0,\dot{v}_0)$. To examine the explicit roles of the load

We investigate equations (5) and (6) for the dependence of the system free response in consequence to various initial values, $(x_0, \dot{x}_0, v_0, \dot{v}_0)$. To examine the explicit roles of the load parameter p that can introduce the system operation at the critical point $p=1$, we focus upon the set $(0, \dot{x}_0, 0, 0)$. By the impulse-momentum theorem, this initial condition set is representative of a sudden impact to the exterior structure (e.g. to the shell by an impact from a rigid plane) when the system is originally at rest. Experimentally, the free fall condition is analogous to this approximation, in the absence of significant aerodynamic turbulence.

The equations (5) and (6) are integrated by a fourth-order, adaptive-time-stepping Runge-Kutta algorithm for a given initial velocity $\dot{x}_0$ and load parameter p combination. Due to the nonlinearity and possibility that post-buckled $p>1$ inclusions may induce different time-dependent responses [25], each parameter combination is considered four times with the resulting free response time averaged among the four results. The free response time is computed to be the time duration required for the initial energy of the system to be reduced to 10^{-6} of its starting value. The parameters used for these evaluations are $f=4$, $\mu=0.5$, $\beta=0.1$, $\gamma_1=0.02$, and $\gamma_2=0.1$. The ratio of frequencies f is set to a value that indicates the lowest eigenfrequency of the unconstrained material inclusion (in plane-strain) is greater than the lowest eigenfrequency of the baseline shell in free oscillation (likewise in plane-strain). The ratio of inclusion to shell mass μ is selected based on measurements of the similar trait. The nonlinearity strength β is a value less than unity in accordance with prior assessments regarding large deflections of beams [36]. The loss factor for the shell $\gamma_1=2\zeta_1$ is significantly smaller than that of the inclusion $\gamma_2=2\zeta_2$ which represents the fact that damping of the primary generalized coordinate of motion for the shell is less than that for the primary radial motion of the inclusion geometry. With these

values both damping ratios, ζ_1 and ζ_2, are sufficiently *underdamped*, while the *effective* damping ratio of the inclusion is what grows substantially due to the near-critical point constraint $p \approx 1$.

Figure S2 exemplifies time series of the structure response x corresponding to the range of parameter combinations considered. Considering cases 1, 2, and 3 that excite the structure with relatively small initial energy, $\frac{1}{2}\dot{x}^2 = 1$, there is a rapid elimination of dynamics for the structure when the load parameter is $p = 1$ when compared to the prolonged oscillations that occur if the parameter is $p = 0.75$ (case 1, pre-buckled inclusion) or $p = 1.25$ (case 3, post-buckled inclusion). The differences among cases 1, 2, and 3 are extraordinary in terms of the energy dissipation capability provided by the variation of near-ness of the inclusion load parameter to the critical point, $p = 1$.

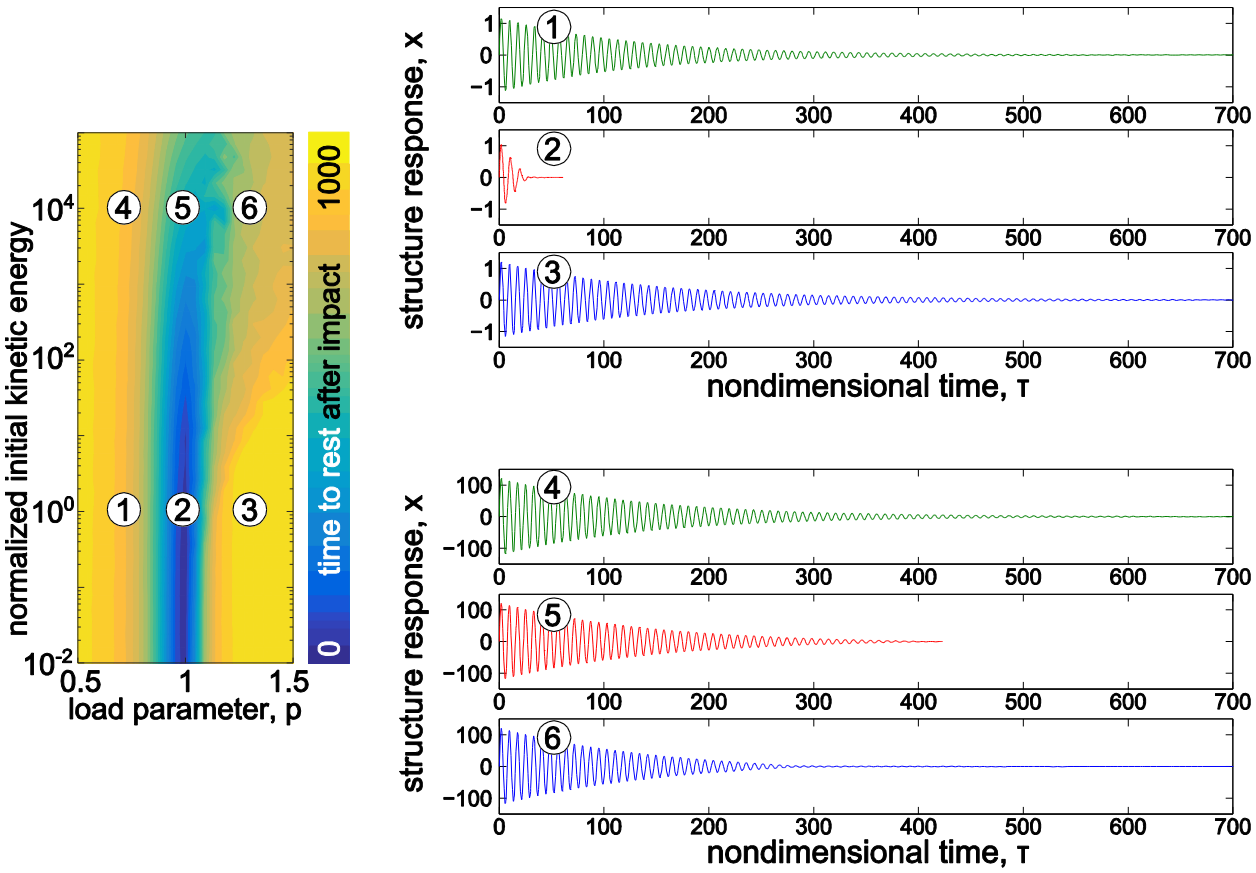

Figure S2. Time series (at right) of structure displacement x corresponding to the individual parameter combinations as labeled in the contour (at left). The complete system parameters used to compute the responses are $f = 4$, $\mu = 0.5$, $\beta = 0.1$, $\gamma_1 = 0.02$, $\gamma_2 = 0.1$.

Considering the cases 4, 5, and 6 that excite the structure with four orders of magnitude greater initial energy, $\frac{1}{2}\dot{x}^2 = 10{,}000$, the free response time is the least when the load parameter is at the critical point (case 5). Yet, although the free response is still less for the case 5 than the cases 4 and 6, the structure response for case 5 is not as dramatically suppressed as that which occurs for the smaller energy input example, case 2. While this indicates that a saturation of the energy dissipation capability may occur for extremely high energy input, one should recall that this simplified model does not take into account alternative failure mechanisms that could become

evident by way of a four order-of-magnitude change in energy input, e.g., plastic deformation in a real system. Putting this in the context of robust, protective material systems, this suggests that material inclusions held near the critical point should be complemented with blast-resistant layers to maximize the effectiveness of an armor across an extreme range of input energies. Importantly, the nondimensionality of the model, equations (5) and (6), provide the means by which to design a material inclusion for the target structure presuming it to not undergo other failure mechanics in the course of its utilization.

2. Material inclusion finite element modeling, fabrication, and specimen preparation

A finite element (FE) model of the architected material inclusion, composed in COMSOL Multiphysics, is utilized to assess the parametric influences that tailor the lowest eigenfrequency and cause it to vanish at the critical point. The FE model is originally developed in the authors' previous work [34] and is employed here to probe a significantly greater parameter space than that considered previously. The FE model geometry is shown at left in Figure 1(d) of the main text and considers the inclusion architecture with seven voids. In this plane strain-based FE model, the outer perimeter of the elastomeric inclusion is compressed in the radial direction normal to the perimeter by the difference between a shell inner diameter D_i =16 mm and a range of inclusion outer diameters D_o that are used in the course of elastomer molding. The diameter ratios D_o / D_i corresponding to this compression range are shown in the axis of FE model results in Figure 1(e) of the main text. In all cases considered, the inner elastomeric core has a constant radius of 3.2 mm while an outer perimeter of the silicone rubber with thickness 1.2 mm is used. Consequently, the change in diameter ratio corresponds to change in the lengths of radially-arrayed beams extending from the elastomeric core while the outer constraint diameter, set by D_i

of the shell dimension, remains fixed. By this model composition, there is no explicit accounting, nor need to account, for the shell mechanics and/or dynamics. A nearly-incompressible, Neo-Hookean, hyperelastic material model is used for the silicone elastomer that composes the inclusions which is a model appropriate for this class of silicone materials [29] [34]. In this case, the strain energy density is $W=\frac{1}{2}\mu_0\left(\bar{I}_1-3\right)+\frac{1}{2}K_0\left(J-1\right)^2$ where μ_0=130 kPa, K_0=130 GPa are the initial shear and bulk moduli, respectively; the Poisson's ratio is ν=0.499; $J=\det\mathbf{F}$ is the determinant of the deformation gradient $\mathbf{F}=\partial\mathbf{x}/\partial\mathbf{X}$ found respecting the current $\mathbf{x}$ and reference $\mathbf{X}$ configurations; $\bar{I}_1=tr\left(\bar{\mathbf{F}}^T\bar{\mathbf{F}}\right)$ is computed from the distortional tensor $\bar{\mathbf{F}}=\left(J^{1/3}\mathbf{I}\right)^{-1}\mathbf{F}$ where $\mathbf{I}$ is the identity matrix; and ρ=1145 kg.m^{-3} is the material density. After meshing the geometry to a fine degree suitably identified via a mesh convergence study, an undamped eigenfrequency analysis evaluates the lowest order eigenfrequencies and how these eigenfrequencies change with respect to variation in the open-to-closed angle ratio α/β and the diameter ratio D_o/D_i. The results of Figure 1(e) are computed over a grid of 21 data points in open angle ratio α/β and 41 data points in diameter ratio D_o/D_i. The increased resolution of computation is applied for the diameter ratio due to observations that it is highly influential upon attaining critical point conditions for small changes in D_o/D_i value.

A 3D printer (FlashForge Creator Pro) is employed to print ABS plastic molds that are the negative of the elastomer elements determined from the FE model. Room-temperature-curing silicone (Smooth-On, Inc., Mold Star 15S) is poured into the molds sprayed with a release agent (Smooth-On, Inc., Ease Release 200). The architected materials are removed after the manufacturer's specified curing time has elapsed. The samples are cut to 50 mm length, and set at room temperature for one week prior to further use. Several samples of a given outer

elastomer diameter D_o are produced (ranging from $D_o \in [16.31,16.78]$ mm). The mean mass of the inclusions is 7.45 g. Aluminum shells of inner diameter D_i =16.00 mm and wall thickness 1.47 mm are cut to 50 mm lengths from a single length of tube (McMaster-Carr 89965K371). To insert the elastomer elements into the shells to realize the specimens with the architected materials constrained near critical points, the inclusions are slightly stretched in their axis to laterally contract them, such that upon release in the shell the inclusions are under the targeted degree of constraint (see Video File 1). Thereafter, the specimens with the architected materials constrained near critical points are considered ready for assessment in the experiments.

3. Experimental methods

The following experimental methods are used to generate the measurements processed for Figures 2, 3, and 4 of the main text and Figure S5. A force transducer (PCB 208C02) is fixed to an aluminum plate of 13 mm thickness. This aluminum plate is bolted to an optical isolation table (Newport Smart Table UT2). A second aluminum plate, 76 mm by 76 mm by 13 mm, is mounted to the top of the force transducer. This upper-most plate serves as the impact surface for the specimens to land upon. This experimental impact plate setup is recommended by the manufacturer for the smaller class of one-dimensional force transducers. All peak forces measured are well within the dynamic range of the transducer. An analog laser displacement sensor (Micro-Epsilon ILD-2300) is directed at the center of the aluminum plate such that as a specimen lands, the laser is pointed at the top edge of the specimen. Specimens are dropped from heights ranging from 135.9 [mm] to 795.9 [mm] above the surface of the impact plate. Specimens are dropped manually such that they fall on an edge and the laser point tracks the opposing edge of the shell. Figure S3 shows the experimental setup for the impact evaluations.

Without touching the plate, foam is placed in the vicinity around the impact plate to protect cabling and other sensitive components. All specimens are dropped at least 40 times from every height. No plastic deformation to the shells is observed in consequence to these experiments.

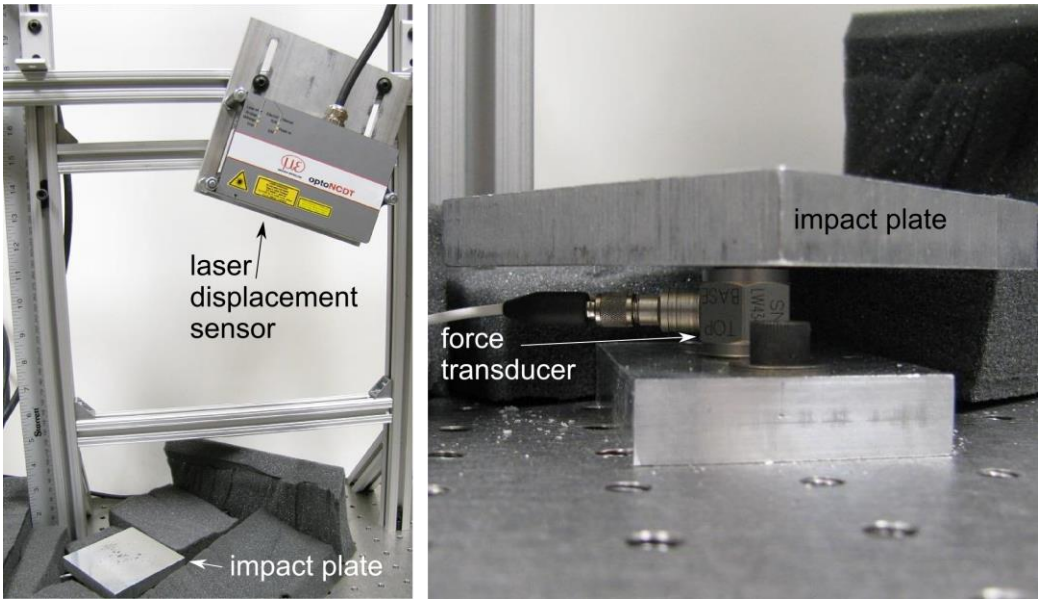

Figure S3. Experimental setup for impact evaluations.

4. Data collection and processing methods

Measurements of impact force and shell displacement are taken at a sampling rate of 131072 Hz using National Instruments data acquisition hardware and the Mathworks MATLAB Data Acquisition Toolbox. Data processing is performed in MATLAB. A digital, second-order Butterworth low pass filter is applied to the measurements at 65536 Hz. The measurements are processed to identify impact events and ensure that the corresponding displacement data for each impact event is permissible. In other words, if the falling shell is sufficiently off-center from the line of the laser then the data is automatically discarded for that impact event. This data assessment procedure inherently removes all impact events that occur off the axis of the force transducer to ensure the force readings are as ideal as possible. Incoming and outgoing shell

velocity respectively are determined from the displacement measurements 20 ms prior and 20 ms following the peak impact forces. The coefficient of restitution (COR) is determined from these associated speeds [35]. The peak impact force is the largest force measurement taken during an impact event. For each case of drop height and specimen as reported in this report, a minimum of 19 and a maximum of 53 corresponding measurements of impact force and shell displacement are approved by the data assessment procedures described above. The mean COR and impact force results and statistics are derived from these measurements.

5. Additional experimental results

In addition to the specimens with material inclusions reported on in the main text, we also fabricate specimens according to the parameter sets provided in Figure S4. The net results from the COR and impact force evaluations are presented in Figure S5(a) and (b), respectively, along with the results for the specimens with the bulk elastomer inclusion and the shell itself. The specimens with material inclusions closest to the critical point have double-thickness lines in the plots, with cyan and light blue colors/markers according to the corresponding notation shown in Figure S4. It is apparent that specimens with architected material inclusions constrained nearer to the critical point (double-thickness lines) are more effective at impact energy absorption by virtue of the reduced COR in Figure S5(a), while the peak impact force exerted upon the strategically designed specimens are all similarly small compared to the specimen with bulk elastomer.

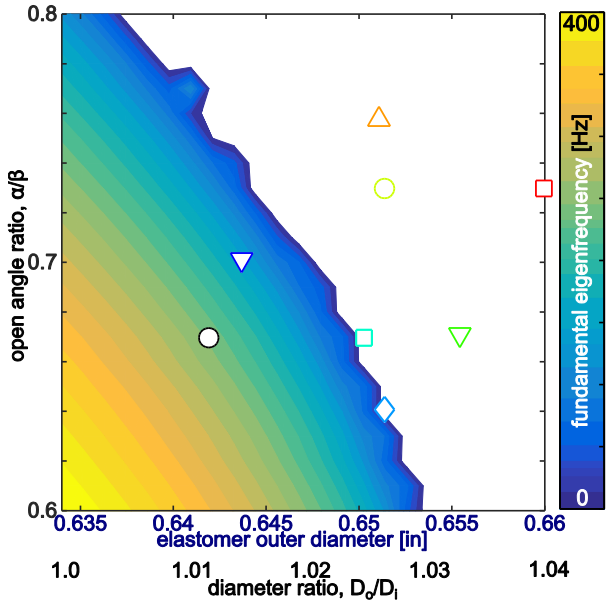

Figure S4. Range of experimentally characterized material inclusion designs, presented according to their respective locations in parameter space ($\alpha / \beta, D_o / D_i$) and FE model lowest eigenfrequency prediction.

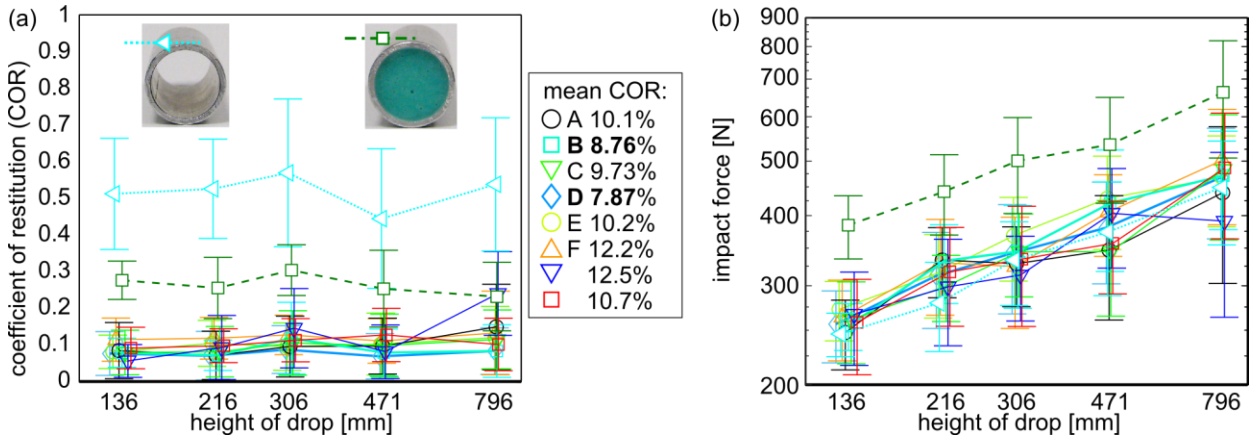

Figure S5. Experimental measurements of (a) COR and (b) impact force for all specimens examined.

Video files descriptions

Video file 1: Once fabricated, the material inclusions are compressed into the cylindrical shells using a fine implement (tweezers are shown in the video as one option) that assists to laterally contract the inclusions upon insertion. Inside of the shell, the inclusions are repositioned by the

implement to ensure that equal fit and compression are achieved inside of the shell. This desired condition is easily assessed via observation of the cross-section following insertion: if the cross-section shows signs of rotation along the length then the inclusion is insufficiently settled into the shell and additional repositioning by the implement is required. Once evenly settled within the shell, the specimen is ready to be examined in experiment.

Video file 2: One-eighth of real-time speed video (recorded at 240 frames per second) of drop experiments conducted using the shell specimen (at left), shell specimen with a fill of the bulk elastomer (at middle), and shell specimen and material inclusion with design parameters $D_o / D_i = 1.03$ and $\alpha / \beta = 0.76$ (at right), from a height of 430 [mm]. The specimens land on the impact plate with force transducer mounted beneath. Representative drop experiments are first shown at full-view, followed by similar representative experiments in close-up-view.

Video file 3: One-eighth of real-time speed video (recorded at 240 frames per second) of drop experiments conducted using the same three specimens as in Video file 2, from a drop height of 5.8 [m]. The specimens land on a solid concrete surface. The right-to-left order of videos is associated with the same specimens as in Video file 2. The experiments are conducted for illustration purposes to investigate a potential saturation-type phenomenon of energy dissipation as observed in the analytical model, Figure S2. Despite increasing the drop height by approximately an order-of-magnitude from those considered in the experiments with results presented in Figures 2, 3, 4, and S5, the specimen with the material inclusion is still substantially suppressed in the rebound response when compared to the other baseline specimens. No saturation-type phenomenon is thus observed over the range of impact energies associated with drop heights from 136 [mm] to 5.8 [m]. In addition, the three specimens do not reveal signs of plastic deformation to the respective shells in consequence to these drops.